International Journal of Fatigue 195 (2025) 108852

Contents lists available at ScienceDirect

International Journal of Fatigue

journal homepage: www.elsevier.com/locate/ijfatigue

Transferability of anomaly data to fatigue properties of PBF-LB AlSi10Mg parts with different volumes

G. Minerva [a], M. Awd [b], A. Koch [c], F. Walther [c], S. Beretta [a,d,*]

[a] Politecnico di Milano, Department of Mechanical Engineering, via La Masa 1, 20156, Milano, Italy
[b] Institute of Informatics and Automation (IIA), Bremen City University of Applied Sciences (HSB), Flughafenallee 10, D-28199, Bremen, Germany
[c] TU Dortmund University, Chair of Materials Test Engineering, Baroper Straße 303, 44227, Dortmund, Germany
[d] Auburn University, National Center for Additive Manufacturing Excellence, Department of Mechanical Engineering, Auburn, AL, 36849, United States of America

ARTICLE INFO

Keywords:
Laser-Powder Bed Fusion
Extreme Value Statistics
Scale effect
Fatigue

ABSTRACT

Fatigue of metallic materials produced by Laser Powder Bed Fusion has been extensively studied for both standard testing specimens and application relevant components. However, fatigue properties of specimens and components suffer from large scatter, mainly due to the presence of volumetric anomalies, residual stresses and surface roughness. Therefore, the transferability from specimens to components is still an open point that must be addressed. In this work, fatigue properties of notched components are investigated and compared with the standard specimens. Then, the properties of the components are inferred from the standard specimens' data using simple models. The maxima anomalies' distributions are estimated with a competing risk approach using Machine learning-assisted Extreme Value Statistics. Finally, the S-N curves of the investigated components, predicted employing the Shiozawa model for finite life and the El-Haddad model for the fatigue limit, closely matched the experimental results.

1. Introduction

Fatigue behaviour of metallic components manufactured by Laser-Powder Bed Fusion (PBF-LB) is certainly one of the most prolific and relevant research field. Numerous studies were devoted to investigate the relationship between fatigue properties and Additive Manufacturing (AM) features, such as process-induced volumetric anomalies, residual stresses and surface roughness [1–6]. These studies lead to the important conclusion that the link between maximum defect and fatigue life, already established for conventional materials [7], exists also for metals manufactured by PBF-LB [8–10]. Therefore, the identification of the so-called "killer" defect which determine component failure is of primary relevance. For failures originated by volumetric anomalies (i.e. gas-entrapped porosity, keyhole porosity, lack-of-fusion (LoF), cluster of pores, etc.) [11–15], X-ray micro-computed tomography (μ-CT scan) has been successfully employed for material characterisation of standard high-cycle fatigue (HCF) specimens. In fact, μ-CT scan has been introduced in recent standards for the qualification of AM processes and components [16], mainly due to the high ratio of information output to cost and time [17,18]. Once the volumetric anomalies population is known, either by sampling on μ-CT scan data [19–21] or on polished sections [19,22,23], Extreme Value Statistics (EVS) allow to model the size-effect, which describes how the maximum defect size changes with the relevant material volume [24,25].

However, when several types of volumetric anomalies are present, then the maxima distributions assume curvilinear shapes and a more complex description is needed [20,25]. The authors showed in [26] that a simple solution to improve the description of maxima distributions is to employ machine learning-assisted EVS. In fact, supervised machine learning (ML) algorithms already proved to be able to provide efficient and fast categorisation of volumetric material anomalies [27–30]. Then, ML algorithms allow to perform EVS for each type of anomaly, which in turn leads to simple and robust maxima distributions [26], resulting independent from the sampling volume. However, after the maxima distributions have been obtained, how to transfer the anomaly data of HCF specimens to fatigue properties of components still remains an open point that needs to be addressed. In fact, while the effect of different types of anomalies on fatigue life has been previously investigated in the literature [31], EVS was not employed to estimate the distribution of anomalies.

This work aims at investigating the effect of different material volumes when multiple defect types are present and extreme value distributions are obtained for each defect type. The relevant material volumes of AM components may be significantly reduced with respect

* Corresponding author at: Politecnico di Milano, Department of Mechanical Engineering, via La Masa 1, 20156, Milano, Italy.
E-mail address: stefano.beretta@polimi.it (S. Beretta).

https://doi.org/10.1016/j.ijfatigue.2025.108852
Received 18 September 2024; Received in revised form 10 January 2025; Accepted 29 January 2025
Available online 10 February 2025

Nomenclature

$\sqrt{\text{area}}$	Square root of the defect's area (Defect size)
$\sqrt{\text{area}_0}$	El-Haddad parameter according to the Murakami's equivalent crack size
α	Constraint factor
γ	Shape parameter of GEVD
$\Delta\sigma$	Stress range
$\Delta\sigma_{loc}$	Local stress range
$\Delta\sigma_{w}$	Fatigue limit in presence of a defect
$\Delta\sigma_{w,0}$	Theoretical endurance limit for the defect-free material
ΔF	Axial load range
ΔK	Cyclic SIF at failure initiating defect
ΔK_1	Cyclic SIF at the long crack threshold for R→1.
$\Delta K_{th,LC}$	Cyclic SIF at the long crack threshold
μ	Location parameter of GEVD and LEVD
ν	Poisson's ratio
σ	Scale parameter of GEVD and LEVD
σ_{loc}	Local peak stress
$\sigma_{\log N_{def}}$	Standard deviation of defect-related life of the Shiozawa curve
$\sigma_{\log \Delta K}$	Standard deviation of cyclic SIF of the Shiozawa curve
σ_{max}	Maximum stress
σ_0	Flow stress
A_0	Parameter of the NASGRO threshold equation
A_1	Parameter of the NASGRO threshold equation
a	Slope of the Shiozawa curve
b	Intercept of the Shiozawa curve
C_{th}^{+}	Parameter of the NASGRO threshold equation
C_{th}^{-}	Parameter of the NASGRO threshold equation
C	Coefficient of Paris–Erdogan curve
d'	Coefficient of Shiozawa curve
E	Elastic modulus
F	Distribution function
K'_f	Coefficient of Shiozawa curve
m	Coefficient of Paris–Erdogan curve
N_f	Number of cycles to failure
N_{def}	Defect-related life
$p_{\%}$	Percentile
P_f	Failure probability
R	Load ratio
R_L	Reliability
V_{BM}	Block Maxima sampling volume
V_{ref}	Prospective material volume
$V_{90\%}$	Volume subjected to 90% to 100% of the highest maximum principal stress in a component
Y	Shape factor

Abbreviations

μ-CT scan	X-ray micro-computed tomography
AM	Additive Manufacturing
BM	Block Maxima
CR	Competing Risk
EVS	Extreme Value Statistics
FE	Finite Element
FEA	Finite Element Analysis
GEVD	Generalized Extreme Value Distribution
GPD	Generalized Pareto Distribution
HCF	High-Cycle Fatigue
HIP	Hot Isostatic Pressing
HL	Cylindrical specimens with hole
ML	Machine Learning
LEVD	Largest Extreme Value Distribution
LoF	Lack-of-Fusion
PBF-LB	Laser-Powder Bed Fusion
POT	Peaks-over-Threshold
SEM	Scanning Electron Microscope
SIF	Stress Intensity Factor
WB	Wishbone specimens

to the large volumes of HCF specimens, due to the presence of complex features and multiple stress concentration locations. Therefore, two notched specimens were developed to investigate small material volumes, calibrated with dedicated Finite Element Analyses (FEA). The notched components were subjected to fatigue testing and the obtained fatigue properties were compared with the standard specimens. Finally, the fatigue properties of the components were inferred from the standard specimens' data using simple models, such as the Shiozawa law and the El-Haddad formulation.

The structure of this paper is the following: Section 2 reports the specimen geometries, the details of the finite element (FE) analyses and the experimental setup. Section 3 describe the EVS model employed to describe volumetric anomalies, while Section 4 reports the results of the notched specimens' fatigue tests and FE analyses, and the killer defect sizes estimated with the EVS model. Fatigue life predictions are reported in Section 5. Finally, conclusions are summarised in Section 6.

2. Materials and methods

The specimens used in this study were fabricated using an SLM 280HL v1.0 system equipped with two 400 W Yttrium fibre lasers working in parallel in a build chamber that measures 280 × 280 × 350 mm^3 (SLM Solution Group AG). The build chamber was flooded with argon to reach oxygen levels lower than 2000 ppm during the printing process. The printing parameters were as follows: beam power P = 350 W, hatch distance h = 0.13 mm and scan speed v = 1650 mm/s. The selected layer thickness was t = 50 μm and produced an energy density of 32.63 J/mm^3. The beam spot size declared by the machine manufacturer ranged from 80 to 115 μm. The building platform was heated up to 150 °C. The scan strategy adopted stripes with width 10 mm rotated by 67 ° after each layer and the scanning order was two contours, followed by the hatch scanning. The parameters were optimised to obtain a minimum density above 99.8%. The presence of lack-of-fusion observed on the fracture surfaces and μ-CT scan of the HCF specimens could be due to several factors, e.g.: the variability of the melt pool [32], the possible presence of spatter on the powder bed [33], the impossibility of controlling the humidity inside the building chamber for the printing machine employed in this study [34]. AlSi10Mg powder, produced by ECKA Granules, was characterised by a mean granule size of 37 μm, D_{10} = 21 μm and D_{90} = 65 μm with a flowability of 80 s/50 g. The specimens were manufactured without supports in different build

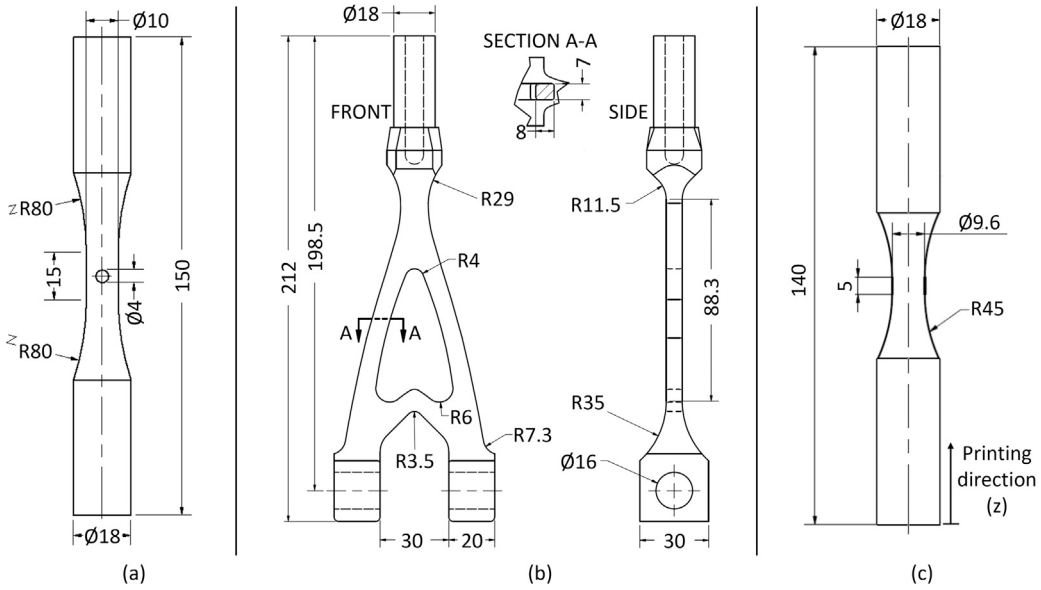

Fig. 1. Geometry of the specimens employed in this study. (a) HL specimen. (b) WB specimen. (c) HCF specimen from [6]. All dimensions are in [mm].

Table 1
Specimens' summary.

Specimen ID	Number of specimens
HL	6
WB	8

jobs, one for each specimen type, covering the whole build platform. Before separating the specimens from the building platform, each build job was subjected to direct ageing heat treatment at 200 °C for 4 h. After the heat treatment, the surface of the specimens was subjected to sand-blasting.

Fig. 1 shows the geometry of the specimens employed in this study:

- cylindrical (HL) specimens, designed according to ASTM E466 [35], with a hole at the centre of the gauge section;
- wishbone (WB) specimens, obtained by modifying the geometry described in [36].
- cylindrical HCF specimens for load controlled testing, extensively describe in [6].

Table 1 provides a summary of the component-like specimens produced in this work.

The WB specimens were originally designed in [36] to have three highly stressed regions: (i) the neck near the upper grip; (ii) the outer surface at the transitions between the two "legs" and the upper grip; (iii) the inner surface of the "legs" at mid height. In the new design, a notch with a depth of 200 μm was introduced in region ii to further reduce the relevant material volume. The bottom section was designed to accommodate a horizontal pin with diameter of 7 mm, while the top section, originally designed with a threaded hole, was characterised by a hollow cylinder. All the specimens were printed with the loading axis aligned with the building direction (z axis). The 4 mm hole of the HL specimens was obtained after printing by micro-Electric Discharge Machining. The two grips of the HL specimens, as well as the top grip and the hole in the lower region of the WB specimens, were machined to guarantee alignment with the machines' fixtures during the fatigue tests.

2.1. Finite element analyses

FEA were carried out using Simulia Abaqus by Dassault Systèmes to estimate the relevant material volume and extract the state of stress acting on the critical locations of the specimens. Linear-elastic material properties were employed for the analyses, with elastic modulus equal to $E = 70\,000$ MPa and Poisson's ratio equal to $\nu = 0.3$. An overall load of 1 kN was applied to both geometries, exploiting the linear-elastic material assumption to scale the obtained states of stress for all the load levels of interest. The relevant material volume V_{ref} was computed as $V_{90\%}$, that is the volume carrying a maximum principal stress between 90% and 100% of the highest maximum principal stress in the component.

2.1.1. Cylindrical specimens

FEA of the HL specimens was developed using a 1/8 model, exploiting the three planes of symmetry of the geometry (Fig. 2). The simulations were carried out with quadratic brick elements (C3D20), with average dimension set to 200 μm near the hole. The FE simulations were performed by applying a remote load to a reference point which was kinematically coupled with the top surface of the specimens, which emulated the loading conditions of the experimental set-up.

2.1.2. Wishbone specimens

FEA of the WB specimens was developed using a 1/4 model, exploiting the xz and yz planes as planes of symmetry (Fig. 3(a)). The simulations were carried out with quadratic tetrahedral elements (C3D10), with average dimension of 250 μm in the stress concentration region. The region of stress concentration was measured employing a Zeiss AxioVision optical microscope and was reproduced in the model (Fig. 3(b,c,d)). The FE simulations were performed by applying a remote load to a reference point which was kinematically coupled with the internal region of the top grip. The pin of the experimental set-up was recreated by kinematically coupling the surface of the hole in the lower portion of the specimen with a reference point lying on the intersection between the hole's axis and the top grip axis, allowing rotation about and sliding along the y axis.

2.2. Fatigue tests

Fatigue tests of HL specimens were conducted on a servo-hydraulic Instron 8801, while tests of WB specimens were conducted on a servo-hydraulic MTS 810 equipped with a 100 kN load cell. All the tests were carried out in force control at 25 Hz under completely reversed loading conditions (i.e. with a load ratio $R = -1$).

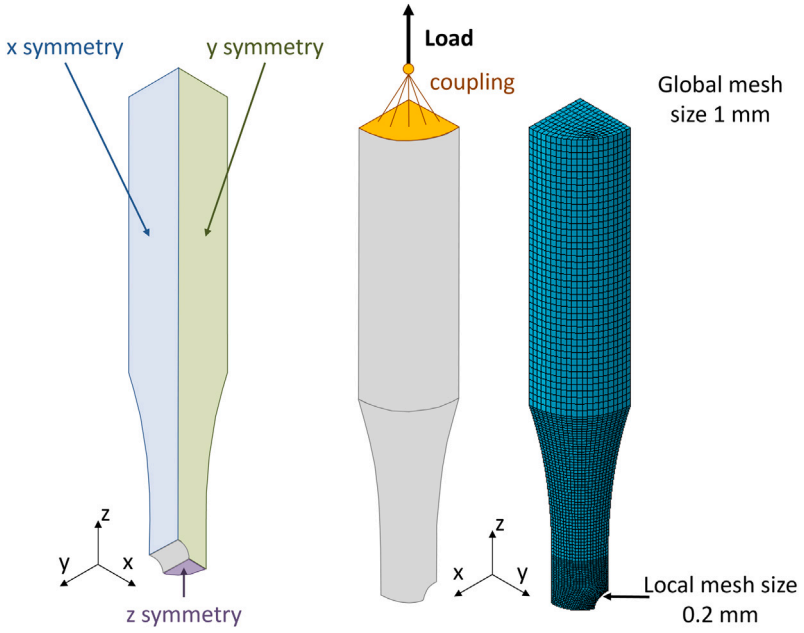

Fig. 2. FE model of HL specimen.

2.3. Fracture analysis

After the fatigue tests, the fracture surfaces of HL specimens were analysed with a Tescan Mira 3 Scanning Electron Microscope (SEM), while a Zeiss Sigma 500 SEM was employed for WB specimens. The size of the anomalies, expressed as $\sqrt{\text{area}}$, was measured with the software ImageJ and for each specimen the largest was identified as the killer defect.

2.4. X-ray micro-computed tomography

Five grip ends of the HCF specimens with an overall volume of 38000 mm^3 were subjected to μ-CT scan to investigate the population of volumetric anomalies. Each μ-CT scan was carried out with a Zeiss Metrotom 1500, employing the following scanning parameters to produce a voxel size of 15 μm: detector pixel pitch of 113 μm, focal spot size of 30 μm, voltage of 210 kV and magnification of x9.3. The voxel size was selected as a trade-off between the size of the investigated volume and the description of the features of the anomalies.

The volumetric anomalies were derived using VGStudio Max software version 3.4.2. Defect identification was carried out with the EasyPore algorithm, employing a relative difference of 80% on the threshold, set as the iso-value 60 of the histogram of intensity. The parameters were selected after a careful visual check on a sub-volume prior to the actual analysis. Finally, a threshold on the minimum anomaly diameter was set at 50 μm, given that the lower limit for an accurate reconstruction is approximately three times the voxel size.

3. EVS model for material anomalies

Process-induced material anomalies are always present in AM components not subjected to Hot Isostatic Pressing (HIP). When multiple anomaly types are present, as is typical for Al-based alloys, directly employing EVS leads to curvilinear anomalies' size distributions (Fig. 4(a)). However, when supervised ML algorithms are employed to efficiently categorise volumetric anomalies (Fig. 4(b)), EVS of each anomaly type produces robust and simple maxima distributions (Fig. 4(c)). The ML-assisted EVS model for volumetric anomalies proposed by the authors in [26] is hereby summarised:

1. Specimens are subjected to μ-CT scan.
2. Internal anomalies are revealed with dedicated post-processors.
3. A selection of anomalies representative of different types are individually classified.
4. A ML algorithm, e.g. a neural network or a decision tree, is trained using the identified anomalies and then employed to classify all the anomalies revealed by μ-CT scan.
5. Sampling is performed separately onto the different types of anomalies.
6. EVS is employed to fit the maxima anomalies' distributions and make predictions onto relevant volumes for each anomalies type.

Considering Block Maxima (BM) sampled anomalies on a sampling volume V_{BM}, the Generalised Extreme Value Distribution (GEVD) can be employed to fit the data. The GEVD has distribution function:

$$F(x) = \exp\left(-\left(1+\gamma\cdot\frac{x-\mu}{\sigma}\right)^{-\frac{1}{\gamma}}\right) \tag{1}$$

where γ is the shape parameter, μ is the location parameter and σ is the scale parameter. For $\gamma = 0$, typical when a single type of anomaly is sampled, the GEVD becomes a Largest Extreme Value Distribution (LEVD) with distribution function:

$$F(x) = \exp\left(-\exp\left(-\frac{x-\mu}{\sigma}\right)\right) \tag{2}$$

After fitting the distributions, a Competing Risk (CR) approach can be employed to account for the presence of multiple types of anomalies [37]. The CR approach models the competition between multiple distributions as independent realisations onto the same reference volume V_{ref}, thus describing the overall cumulative distribution function F_{CR} for the anomalies' size as:

$$F_{CR}(x) = \prod_i F_i(x) = \exp\left(-\sum\exp\left(-\frac{x-\mu_i-\sigma_i\cdot\log(V_{ref}/V_{BM,i})}{\sigma_i}\right)\right) \tag{3}$$

where the subscript i refers to the i_{th} anomaly type.

The effect of the volume is governed by the parameter σ, which is an index of the scatter of the distribution. For large values of σ, the size distribution changes significantly over different volumes, while for small values of σ the distribution is less affected.

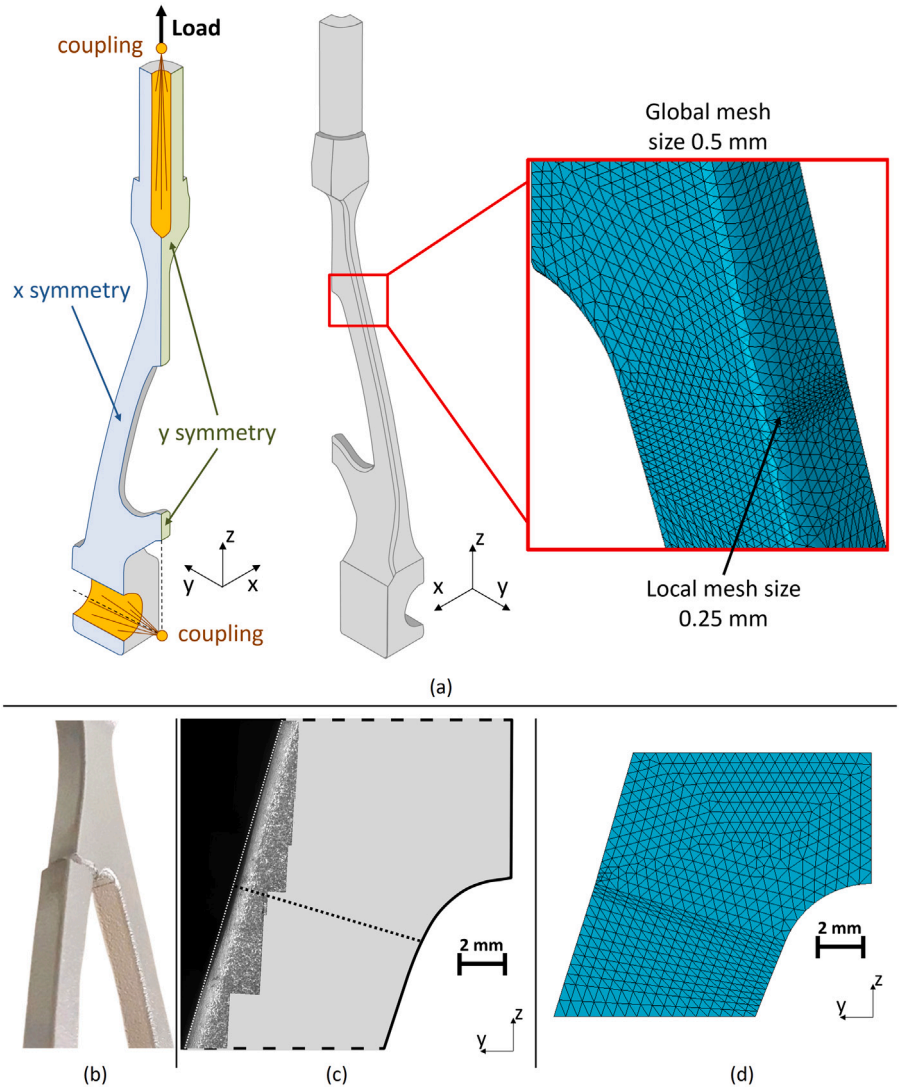

Fig. 3. FE model of WB specimen. (a) Symmetries, boundary conditions and size of the mesh. (b) Example of failed WB specimen. (c) Region of the notch, in which the plane normal to the surface is shown with a dotted black line. (d) Detail of the mesh of the FEM near the notch of WB specimens.

It is important to highlight that the CR approach is effectively a weakest link model. In fact, let us consider the relationship between a target life $N_f(\bar{a})$ and the related initial defect size $\bar{a}$, which can be derived with suitable fatigue models and is schematically shown in Fig. 5. The failure probability at the target life $N_f(\bar{a})$ is defined as:

$$P_f = \Pr[N_f \leq N_f(\bar{a})] \tag{4}$$

Considering that the relationship between $N_f(\bar{a})$ and $\bar{a}$ is monotonic, it follows that:

$$\Pr[N_f \leq N_f(\bar{a})] = \Pr[a > \bar{a}] \tag{5}$$

And thus:

$$P_f = 1 - F(\bar{a}) \tag{6}$$

Rewriting Eq. (6) in terms of reliability $R_L = 1 - P_f$ and considering for the distribution of the defect size with the CR approach, it follows that:

$$R_L = F_{CR}(\bar{a}) = \prod_i F_i(\bar{a}) = \prod_i R_{L,i} \tag{7}$$

Which is the formulation for the reliability of a series system, i.e. a weakest link model for failure.

Table 2
Parameters of LEVDs for maxima pores and LoFs from [26].

Anomaly type	μ [μm]	σ [μm]	V_{BM} [mm^3]
Pores	109.30	9.20	127
LoFs	87.97	37.58	127

In this work, the volumetric anomalies' distributions of HCF specimens manufactured by PBF-LB in AlSi10Mg and reported in [26] were considered. In fact, the material was nominally the same as the one of the present study (i.e. the specimens were printed by the same company, employing the same machine and printing parameters, and underwent the same heat treatment). After the defect identification, BM sampling was carried out on the cylindrical volumes, employing sampling disks of height h = 0.5 mm, thus defining a sampling volume V_{BM} = 127 mm^3. The largest pore and irregularly shaped anomaly (i.e. LoF or pores' cluster) in each disk were recorded and then fitted with the LEVD, producing the fitting parameters reported in Table 2. The LoFs and pores' clusters were grouped together in the "LoFs" category due to the consistent overlap of the features employed for their description.

The importance of applying a CR approach is well captured by Fig. 6, which provides a comparison between the CR approach and

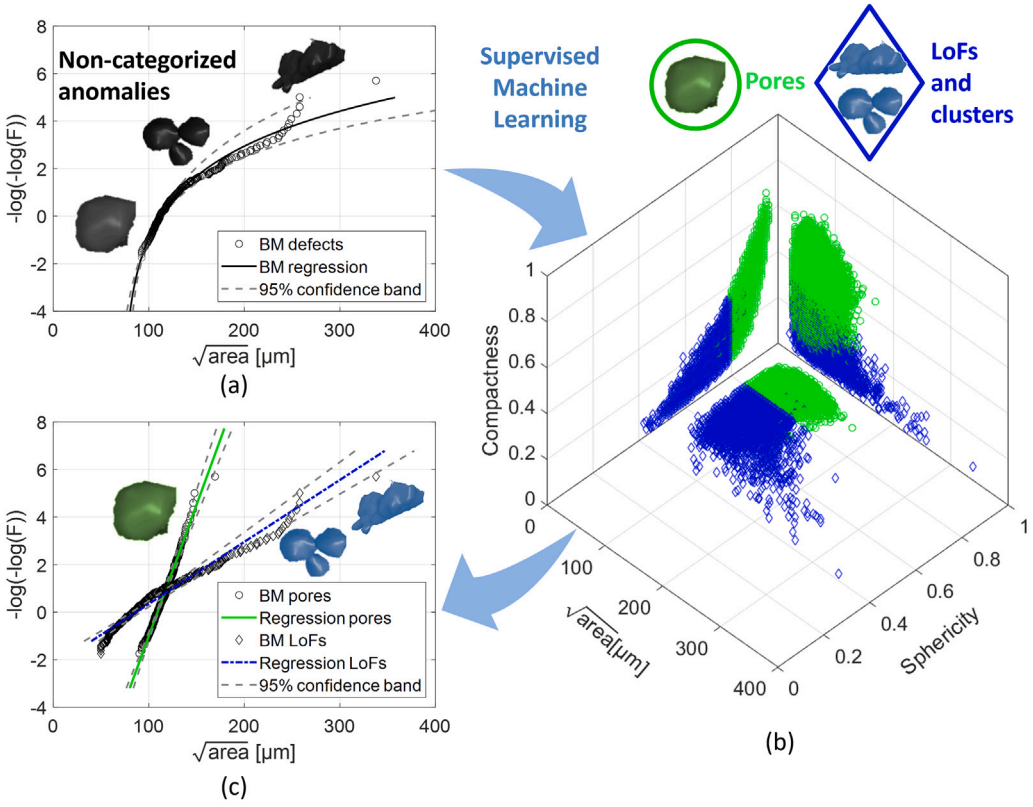

Fig. 4. (a) GEVD with non-categorised anomalies. (b) Features of pores and irregular anomalies (i.e. LoFs and clusters of pores) categorised with a decision tree algorithm. (c) LEVDs of pores and irregular anomalies after categorisation.
Source: Adapted from [26].

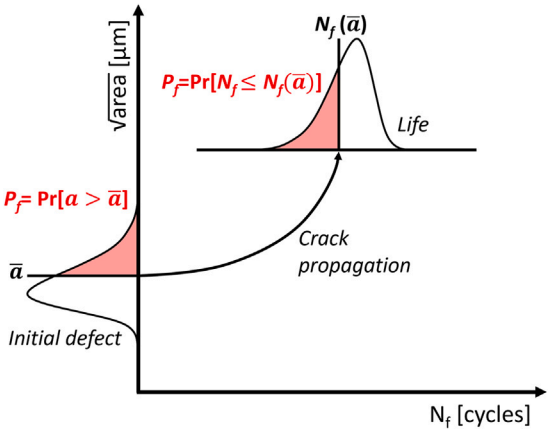

Fig. 5. Scheme of the relationship between failure probability for a target number of cycles and initial defect size distribution.

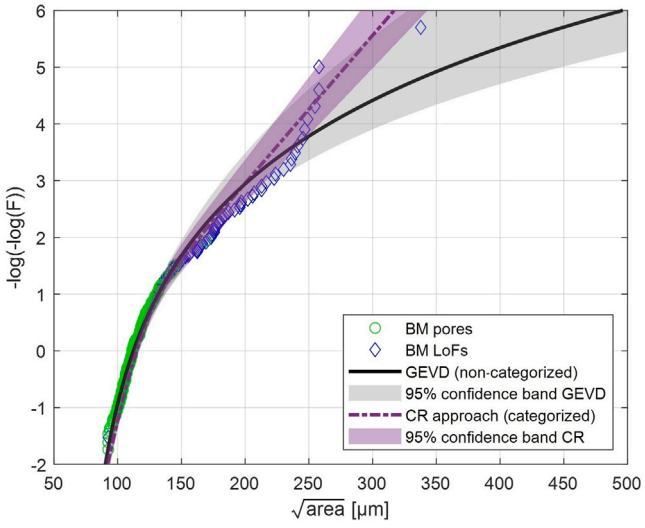

Fig. 6. Comparison of 95% confidence bands for GEVD on non-categorised anomalies and CR approach on categorised anomalies.

the GEVD on the non-categorised anomalies with their 95% confidence bands. In fact, while the confidence band of the GEVD becomes very large for large percentiles, the confidence band for the CR approach remains narrow and close to the largest sampled anomalies.

It is important to underline that for materials with low defect density the BM approach would need to be applied properly, so that the maxima are representative of the material (i.e. each control volume for block maxima should contain at least 10–15 anomalies [38]). Two strategies could be applied in this sense: (i) to increase the sampling volume; (ii) to improve the resolution of the µ-CT scan, so that smaller anomalies could be properly identified.

An alternative would be to apply peaks-over-threshold (POT) sampling. However, if the Generalised Pareto Distribution (GPD) is fitted to POT data of non-categorised anomalies [20], the same problems of directly fitting a GEVD to BM data would arise. For example, if only the upper tail of the parent distribution is fitted, only large anomalies (usually LoFs) would be sampled with POT, while pores distribution would be completely lost. On the other hand, if anomalies are categorised, then POT would lead to exponential distributions [37] for which the CR approach can be applied.

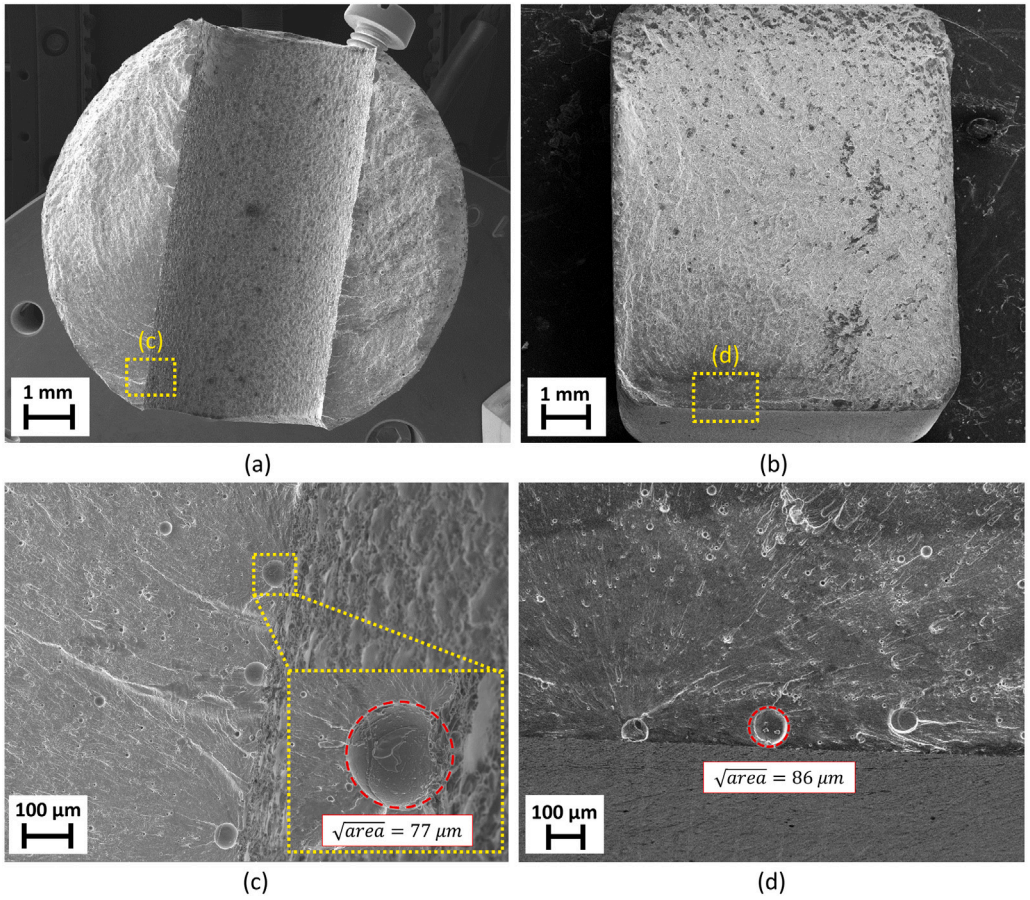

Fig. 7. (a) Fractography of specimen HL5. (b) Fractography of specimen WB2. (c) Detail of the killer pore of specimen HL5. (d) Detail of the killer pore of specimen WB2.

Table 3
Summary of fatigue test results and fractographies of HL specimens.

Specimen ID	ΔF [kN]	$\Delta\sigma_{loc}$ [MPa]	N_f [cycles]	$\sqrt{area}$ [µm]	Defect type
HL1	6.160	330	37 061	66	Pore
HL2	6.160	330	35 505	94	Pore
HL3	6.160	330	42 884	56	Pore
HL4	6.160	330	37 165	53	Pore
HL5	6.160	330	39 942	77	Pore
HL6	6.468	346	38 840	78	Pore

Table 4
Summary of fatigue test results and fractographies of WB specimens.

Specimen ID	ΔF [kN]	$\Delta\sigma_{loc}$ [MPa]	N_f [cycles]	$\sqrt{area}$ [µm]	Defect type
WB1	15.0	248	57 767	129	Cluster
WB2	15.0	248	232 578	86	Pore
WB3	15.0	248	105 837	80	Pore
WB4	15.0	248	137 057	124	Cluster
WB5	18.8	310	35 570	78	Cluster
WB6	18.8	310	37 543	91	Pore
WB7	18.8	310	39 767	81	Pore
WB8	18.8	310	36 803	99	Pore
WB6	11.0	182	5 000 000 (R.O.)	–	–

4. Results

4.1. Fatigue tests and fractographies

The results of the fatigue tests in terms of applied load ΔF, local stress range $\Delta\sigma_{loc}$ (from FEA), number of cycles at failure N_f, killer defect size $\sqrt{\text{area}}$ and type are reported in Tables 3 and 4, respectively for HL and WB specimens. Exemplary fracture surfaces of HL and WB specimens are shown in Fig. 7, in which the killer defects were highlighted with a red dashed line.

4.2. Finite element analyses

Local peak stress σ_{loc} and relevant material volume V_{ref}, needed for the fatigue life predictions, were estimated from the FEA of HL and WB specimens and are reported in Table 5. Fig. 8 shows the states of stress on the plane perpendicular to the stress concentration features of HL and WB specimens, with σ_{loc} evidenced. Exemplary expected locations of the critical defect and the related initial crack are also shown.

Table 5
Peak stress for 1 kN σ_{loc} and relevant material volume $V_{90\%}$ extracted from FEA of HL and WB specimens.

Specimens	σ_{loc} [MPa]	V_{ref} [mm^3]
HL	53.5	2.9
WB	16.5	28.1

4.3. Killer defect estimates with EVS

The killer defect sizes of HL and WB specimens were fitted with LEVD employing the moments method [39], which minimises the difference between the observed moments of the sample data and the analytical moments of the distribution. On the other hand, the killer defect sizes of HCF specimens were fitted with a GEVD employing the maximum likelihood method [40], which allows to estimate the parameters by maximising the probability that the sample data belongs to the chosen distribution. The fitted parameters are reported in Table 6,

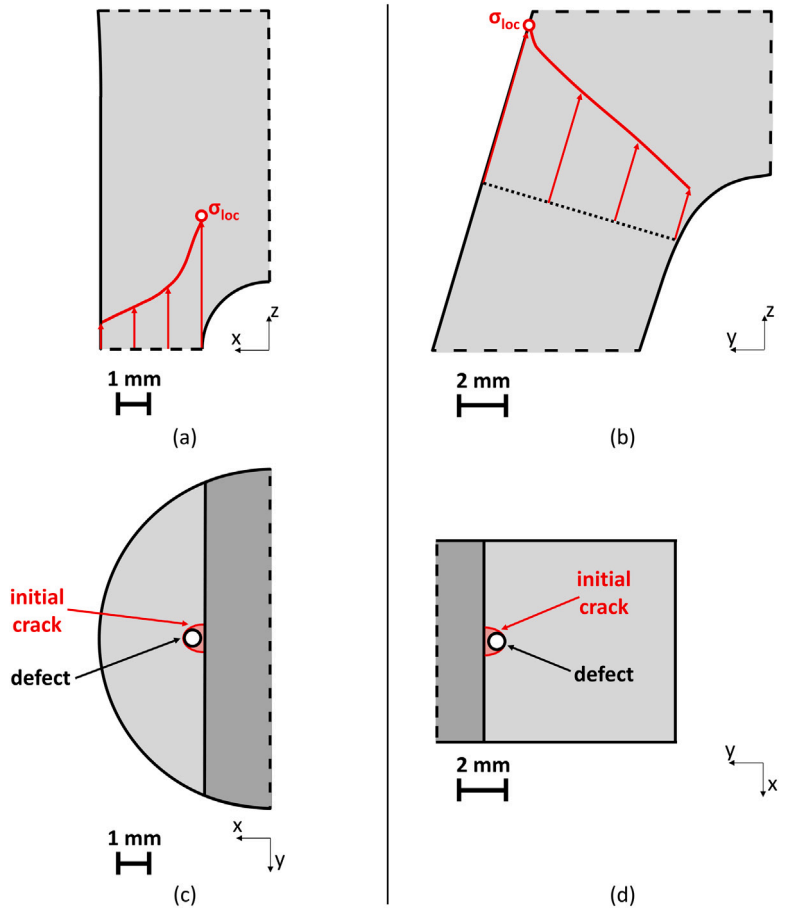

Fig. 8. (a) State of stress in HL specimens. (b) State of stress in WB specimens. (c) Location of critical defect and initial crack for HL specimens. (d) Location of critical defect and initial crack for WB specimens.

Table 6
Estimated parameters of EV distributions for killer defects of HL, WB and HCF specimens.

Specimens	γ [−]	μ [μm]	σ [μm]
HL	0	63.73	12.02
WB	0	87.58	14.59
HCF	0.3565	73.08	16.72

while Fig. 9(a,c,e) show the killer defect distributions of HL, WB and HCF specimens with their 95% confidence band on Gumbel probability charts.

The killer defect sizes of HL and WB specimens were estimated with the CR approach using with the reference volumes V_{ref} calculated with the FEA (Table 5). The resulting distributions are shown in Fig. 9 for HL and WB specimens as well as for the HCF specimens. It is interesting to see that the dispersion (σ) of HL and WB distributions is similar to the dispersion of the pores' distribution of HCF specimens, thus confirming that the distributions obtained from HCF specimens well represent the volumetric anomalies of this AlSi10Mg. This matches the findings from [41], which shows that, while the defect density may change from one specimen to another on the build plate, the technological firm of a process is well captured by the scatter of the distributions, which remains constant.

In Fig. 9(b,d,f) the killer defects of HL, WB and HCF specimens are compared with the pores' and LoFs' probability density function as well as their combination with the CR approach. In this way, it is possible to see the effect of the different relevant volumes on the shift of the pores' and LoFs' distributions.

This well depicts the importance of the CR approach. In fact, while for relatively large material volumes (i.e. for the HCF specimens) both pores and LoFs have distributions with size above 0 μm. For smaller material volumes (i.e. for the WB specimens), part of the LoFs and clusters distribution is below 0 μm, and the ratio of irregular defects to pores is reduced. Finally, for very small material volumes (i.e. $V_{ref} = 2.9$ mm^3 of HL specimens), only the pores distribution is relevant, given that the LoFs and clusters distribution is mostly below 0 μm. This effect is due to the significantly different values of σ of the two distributions, as previously mentioned, and demonstrates the importance of combining the distributions of pores and LoFs to properly capture the occurrence of both for different relevant material volumes.

5. Fatigue life predictions

It has been considerably demonstrated that volumetric anomalies act like short cracks [2,4,6,36,42,43]. Therefore, two defect-based models were considered for fatigue life predictions, namely, Shiozawa law for finite life and El-Haddad model for infinite life, described in the following.

5.1. Finite life model

The Shiozawa law [44] was successfully employed on PBF-LB AlSi10Mg [26,45,46] for fatigue assessment based on stress amplitude and defect size and location. Under the assumptions that the fatigue life is dominated by crack propagation rather than by crack initiation and that the failure-initiating defects are relatively small compared to the crack size at failure, it is possible to integrate the Paris–Erdogan law from the initial defect size $\sqrt{\text{area}}$ to the final crack size. The Shiozawa

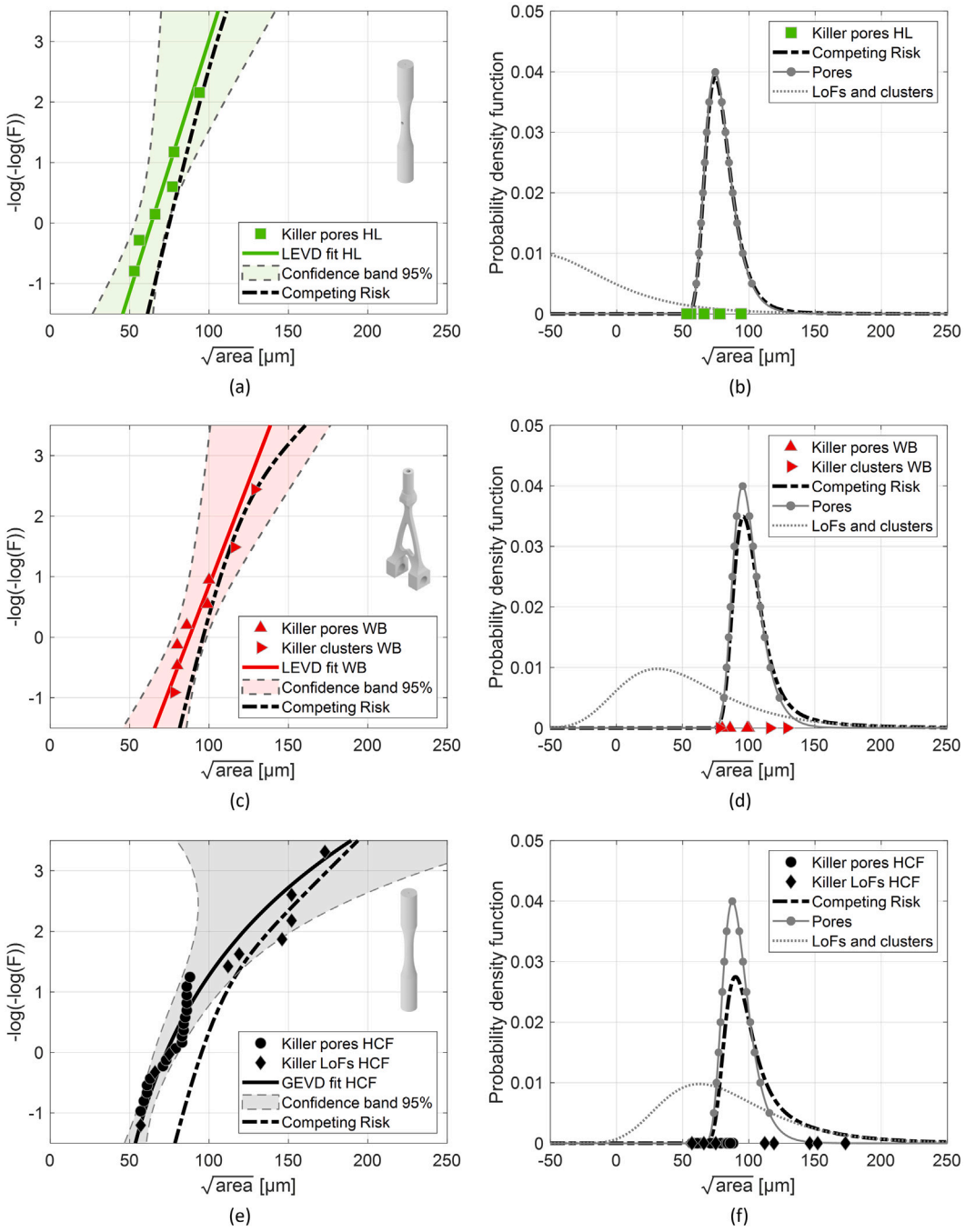

Fig. 9. Comparison between EV distributions of killer defects and the competing risk model on Gumbel probability chart and as probability density function for: (a,b) HL specimens; (c,d) WB specimens; (e,f) and HCF specimens from [6].

law is thus obtained:

$$\Delta K = \left[\frac{C(m-2)}{2}\right]^{-1/m} \cdot \left(\frac{N_f}{\sqrt{\text{area}}}\right)^{-1/m} \tag{8}$$

Defining the defect related life N_{def} as the ratio between the number of cycles to failure N_f and the killer defect size $\sqrt{\text{area}}$, Eq. (8) defines a linear relationship in double logarithmic scale between N_{def} and cyclic SIF ΔK. The ΔK can be estimated with Murakami's formula [42]:

$$\Delta K = \Delta\sigma \cdot Y \cdot \sqrt{\pi \cdot \sqrt{\text{area}}} \tag{9}$$

where the shape factor Y is equal to 0.65 for surface defects and to 0.5 for internal defects. Then, it is possible to fit the Shiozawa curve onto the experimental data assuming N_{def} is log-normally distributed with law:

$$N_{def} \sim \log \mathcal{N}\left(a \cdot \log \Delta K + b, \sigma_{\log N_{def}}\right) \tag{10}$$

where a and b are the fitting parameters of the average Shiozawa curve (50% percentile), while $\sigma_{\log N_{def}}$ is the fitted standard deviation, assumed constant for all levels of ΔK. The fitting was performed by employing the maximum likelihood method [40]. The fitted parameters for the HCF specimens (Fig. 10(a)) are reported in Table 7 and were obtained considering $\sqrt{\text{area}}$ expressed in [m]. The standard deviation in terms of ΔK ($\sigma_{\log \Delta K}$) was also calculated as:

$$\sigma_{\log \Delta K} = -\frac{\sigma_{\log N_{def}}}{a} \tag{11}$$

Table 7
Estimated parameters of Shiozawa curve for the investigated PBF-LB AlSi10Mg.

a	b	$\sigma_{\log N_{def}}$	$\sigma_{\log \Delta K}$
−6.555	27.832	0.633	0.097

Table 8
Parameters of NASGRO equation for long crack threshold of this AlSi10Mg.
Source: From [36].

ΔK_1 [MPa$\sqrt{\text{m}}$]	C_{th}^{+} [−]	C_{th}^{-} [−]	α [−]	σ_{max}/σ_0 [−]
1.0741	−0.5408	0.124	1.9	0.3

It is promising to see how the experimental results for WB and HL specimens lie close to the average Shiozawa curve of the HCF specimens.

Shiozawa law allowed to compute fatigue life for a given combination of load level $\Delta\sigma$ and defect size $\sqrt{area}$ by employing the following equation:

$$N_f = \sqrt{\text{area}} \cdot \exp\left[a \cdot \log\left(Y \cdot \Delta\sigma \cdot \sqrt{\pi \cdot \sqrt{\text{area}}}\right) + b\right] \tag{12}$$

5.2. Fatigue limit model

The El-Haddad formulation of the Kitagawa–Takahashi diagram was employed to model the fatigue limit of the present AlSi10Mg alloy:

$$\Delta\sigma_w = \Delta\sigma_{w,0} \cdot \sqrt{\frac{\sqrt{\text{area}_0}}{\sqrt{\text{area}} + \sqrt{\text{area}_0}}} \tag{13}$$

where the fatigue limit for the defect-free material $\Delta\sigma_{w,0} = 315.8$ MPa (valid for $R \leq -1$) from [6] was considered, while the El-Haddad parameter $\sqrt{\text{area}_0}$ was computed as:

$$\sqrt{\text{area}_0} = \frac{1}{\pi} \cdot \left(\frac{\Delta K_{th,LC}}{Y \cdot \Delta\sigma_{w,0}}\right)^2 \tag{14}$$

The threshold SIF $\Delta K_{th,LC}$ was estimated with the NASGRO equation for long crack threshold for load ratio $R \leq 0$ (Eq. (15)), employing the fitted parameters from [36], reported in Table 8.

$$\begin{cases} \Delta K_{th,LC}(R) = \dfrac{\Delta K_1}{(1-A_0)^{C_{th}^{+}-R\cdot C_{th}^{-}}} \cdot \left(\dfrac{1-R}{1-A_0-A_1\cdot R}\right)^{1+R\cdot C_{th}^{-}} \\ A_0 = \left(0.825 - 0.34\cdot\alpha + 0.05\cdot\alpha^2\right)\cdot\left(\cos\left(0.5\cdot\pi\cdot\dfrac{\sigma_{max}}{\sigma_0}\right)\right)^{1/\alpha} \\ A_1 = (0.415 - 0.071\cdot\alpha)\cdot\dfrac{\sigma_{max}}{\sigma_0} \end{cases} \tag{15}$$

An effective load ratio $R \approx -2$ was considered for the HCF specimens, which accounted for the residual stresses due to machining operations [6]. The same effective load ratio was employed also for the WB specimens, considering compressive residual stresses on the surface due to sand-blasting. Moreover, the residual stress profiles of sandblasted HCF specimens were similar to the profile of machined HCF specimens [47]. On the other hand, the nominal load ratio $R = -1$ was considered for the calculation of the fatigue limit of the HL specimens, due to the fact that the failures originated from the internal surfaces of the hole, which was not subjected to sand-blasting.

5.3. Fatigue life predictions with EVS

For each geometry, defect sizes corresponding to percentiles 2.5%, 50% and 97.5% were used as input for the Shiozawa law to estimate the average S-N curves and a 95% scatter in fatigue life. Analogously, the same percentiles were employed for the El-Haddad model to obtain the average fatigue limit and its 95% scatter. For both formulations, the shape factor Y was always assumed equal to 0.65, i.e. only surface defects were considered. The percentiles estimated with the CR approach are reported in Table 9 for the three series alongside the percentile estimated employing only the pores distribution. The resulting S-N curves using the CR approach and the pores' distribution for HL, WB and HCF specimens are shown in Fig. 10(b,c,d), respectively. It is interesting to see how the S-N curves predicted considering only the pores distribution significantly overestimate the fatigue life of WB and HCF specimens, in which pores' clusters and LoFs were present. On the other hand, predictions with the CR approach well describe the scatter of the fatigue life observed experimentally for all the investigated series.

Table 9
Comparison between percentiles $p_{2.5}$, p_{50}, $p_{97.5}$ of competing risk distribution and pores LEVD, estimated on V_{ref} for HL, WB and HCF specimens.

Specimens	Competing risk [μm]			Pores [μm]		
	$p_{2.5}$	p_{50}	$p_{97.5}$	$p_{2.5}$	p_{50}	$p_{97.5}$
HL	62	78	113	62	78	108
WB	84	101	170	83	99	129
HCF	77	98	201	76	90	121

Additional considerations on the estimated fatigue behaviour when considering also the intrinsic scatter of the Shiozawa model are provided in Appendix.

6. Conclusions

This work investigated the transferability of anomaly data from specimens to components manufactured by PBF-LB in AlSi10Mg. When multiple types of anomalies are present in the material, it is possible to employ Machine-Learning assisted Extreme Value Statistics to obtain individual distributions. Then, employing a Competing Risk approach, it is possible to evaluate the size effect of each distribution onto the components' relevant material volume, estimated with dedicated Finite Element Analyses. Combining Competing Risk estimates with simple defect-based models such as the Shiozawa law and the El-Haddad formulation, the predicted fatigue properties of the investigated component-like specimens were quite close to the experimental results. The following conclusions can be drawn:

- Different material volumes may have significantly different anomaly populations. This is particularly relevant for small material volumes, typical of notched AM components, which lack "rare" anomalies but always contain gas entrapped porosity.
- The Competing Risk approach allows to account for the concurring presence of different types of anomalies with a weakest link model. Moreover, the different effect of the relevant volumes on the anomaly distributions is properly described. For example, if only the largest anomalies were considered (i.e. the LoFs) their size tends to 0 for small volumes. In contrast, when a Competing Risk approach is employed, the overall defect distribution would always have a lower limit provided by the maximum pores, which do not change significantly with the volume of the material, because their dispersion (expressed by the σ parameter) is quite small.
- The Shiozawa model allows to predict fatigue life in a simple way, while accounting for the position and size of the defects. In this work, the Shiozawa model fitted on HCF specimens' data was found to provide accurate estimates for the two component-like geometries. When a Competing Risk approach is employed to estimate the maxima anomalies' size for the relevant material volume, the effect of the different types of anomalies is also correctly captured.

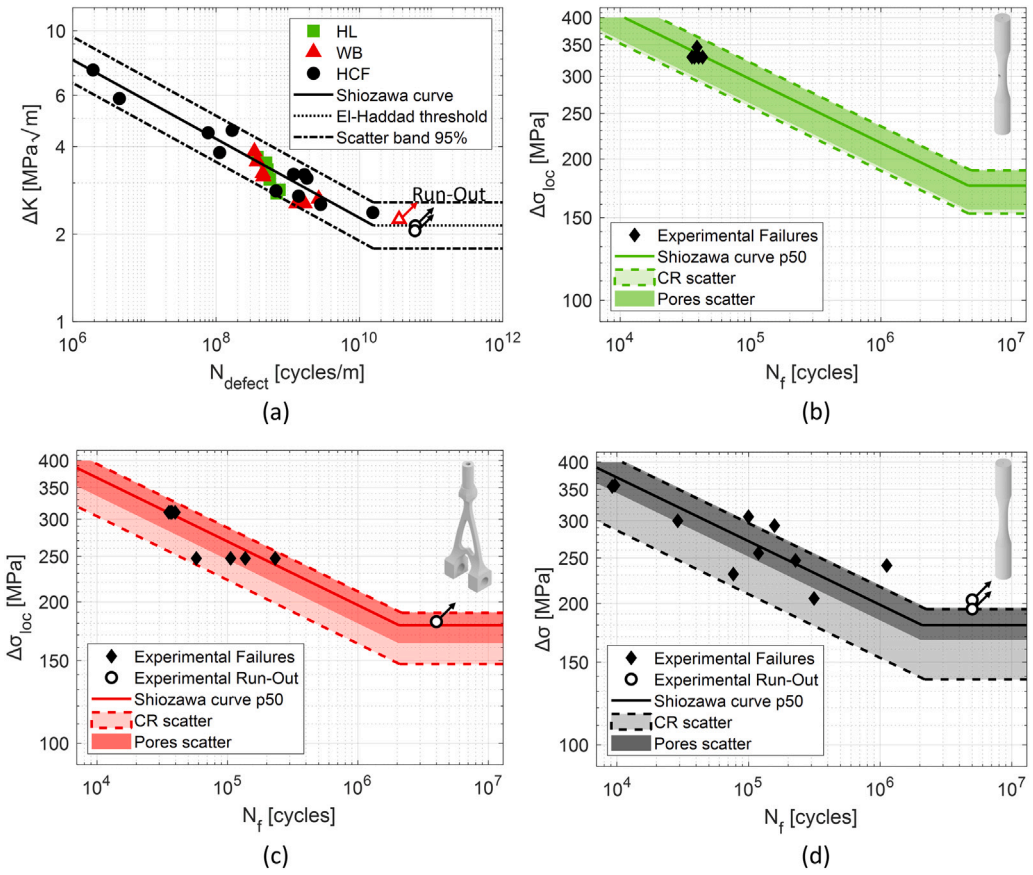

Fig. 10. Shiozawa model for fatigue life considering only the scatter due to defects. (a) Shiozawa curve with the experimental data and the threshold SIF of the El-Haddad model. (b) Experimental data and predicted SN curves for HL specimens. (c) Experimental data and predicted SN curves for WB specimens. (d) Experimental data and predicted SN curves for HCF specimens from [6].

CRediT authorship contribution statement

G. Minerva: Writing – review & editing, Writing – original draft, Methodology, Data curation. **M. Awd:** Writing – review & editing, Supervision, Methodology. **A. Koch:** Writing – review & editing. **F. Walther:** Writing – review & editing, Data curation, Conceptualization. **S. Beretta:** Writing – review & editing, Project administration, Methodology, Investigation, Formal analysis, Conceptualization.

Declaration of competing interest

The authors declare the following financial interests/personal relationships which may be considered as potential competing interests: Frank Walther reports financial support was provided by Deutsche Forschungsgemeinschaft. If there are other authors, they declare that they have no known competing financial interests or personal relationships that could have appeared to influence the work reported in this paper.

Acknowledgements

The authors would like to thank BEAMIT (Fornovo, Italy) for preparing the specimens tested in this research. The Italian Ministry of Education, University and Research is also acknowledged for the support provided through the Project "Department of Excellence LIS4.0 - Lightweight and Smart Structures for Industry 4.0". The authors thank the German Research Foundation (Deutsche Forschungsgemeinschaft, DFG) for its financial support within the research projects "Identification and modeling of damage mechanisms in Al-Si-Mg cast alloys during HCF and VHCF" (No. 282318703), "Mechanism-based assessment of the influence of powder production and process parameters on the microstructure and the deformation behavior of SLM-compacted C+N steels in air and in corrosive environment" (No. 372290567), "Microstructure and defect controlled additive manufacturing of gamma titanium aluminides for function-based control of local materials properties" (No. 404665753) and "Mechanism-based investigation of additively-manufactured aluminum matrix composites (AMC) for enhanced mechanical strength" (No. 425479688).

Appendix. Uncertainty quantification for the Shiozawa model

Within a probabilistic framework, an important factor affecting the predictions is the intrinsic scatter of the chosen model. The intrinsic scatter can be accounted for with suitable statistics tools, such as Monte Carlo (MC) simulations [48]. For the finite life fatigue model provided by Shiozawa's law, this translates to the derivation of the intrinsic scatter from the fitted data ($\sigma_{\log \Delta K}$ in Eq. (11)) and the estimate of maxima anomalies distribution on the relevant material volume.

MC simulations were performed to derive SN curves for the investigated specimens considering only surface defects (i.e. $Y = 0.65$) employing the following procedure:

1. extraction of the killer defect size $\sqrt{\text{area}}$ from the maxima anomalies distributions combined with the CR approach;
2. extraction of the applied SIF range ΔK from the intrinsic scatter of the Shiozawa's model, considering the stress level and the killer defect size.
3. identification of the number of cycles to failure N_f from Eq. (12) for the extracted $\sqrt{\text{area}}$ and ΔK.

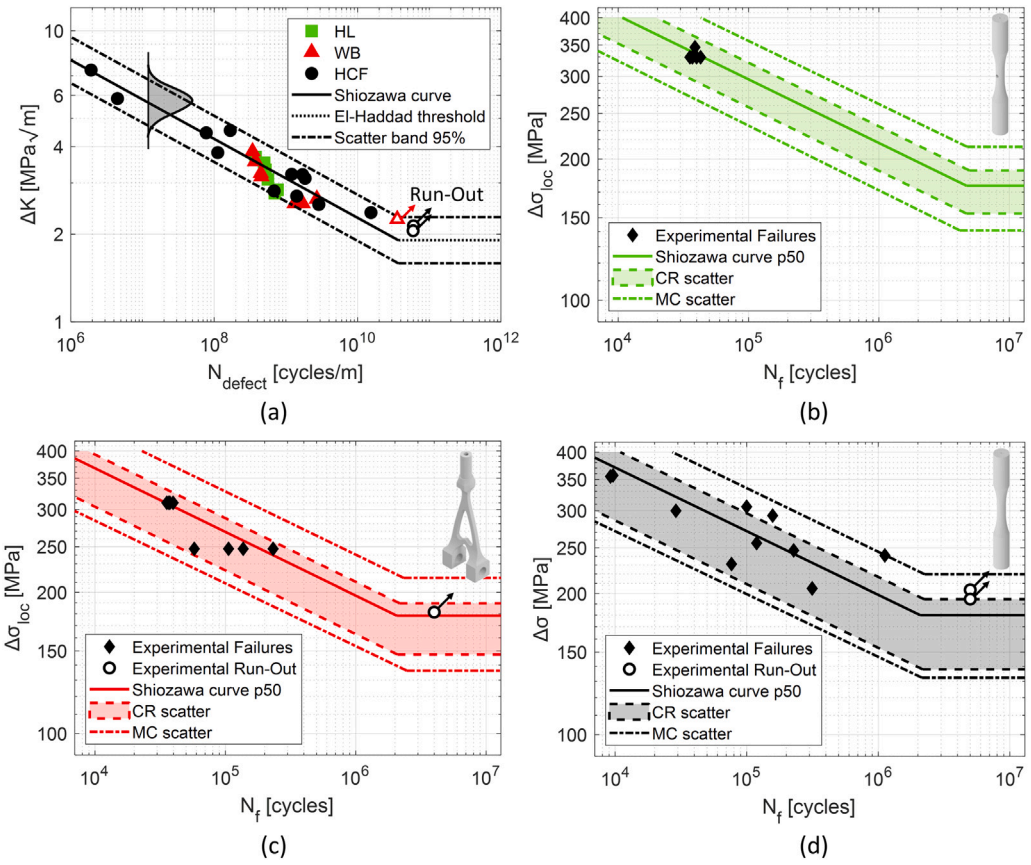

Fig. A.1. Shiozawa model for fatigue life considering the scatter due to the fitting model and the defects. (a) Shiozawa curve with the experimental data and the threshold SIF of the El-Haddad model, highlighting the scatter of the Shiozawa curve along the ΔK axis. (b) Experimental data and predicted SN curves for HL specimens. (c) Experimental data and predicted SN curves for WB specimens. (d) Experimental data and predicted SN curves for HCF specimens from [6].

4. calculation of the percentiles 2.5%, 50% and 97.5% from the distribution of N_f obtained from all the simulations at the given $\Delta\sigma$.
5. definition of the finite life SN curve for different stress level.
6. plot of the scatter bands for the endurance limit estimated with the El-Haddad model using the same scatter identified for the finite life.

The results of the MC simulations are reported in Fig. A.1. It is possible to see how the scatter bands become significantly larger when employing MC simulations, with respect to the scatter bands with only the maxima anomalies distributions and this shows the importance of proper modelling for the scatter of the chosen fatigue model when employing probabilistic approaches.

Data availability

Data will be made available on request.

References

[1] Yadollahi A, Shamsaei N. Additive manufacturing of fatigue resistant materials: Challenges and opportunities. Int J Fatigue 2017;98:14–31. http://dx.doi.org/10.1016/j.ijfatigue.2017.01.001, URL https://linkinghub.elsevier.com/retrieve/pii/S0142112317300014.

[2] Romano S, Brückner-Foit A, Brandão A, Gumpinger J, Ghidini T, Beretta S. Fatigue properties of AlSi10Mg obtained by additive manufacturing: Defect-based modelling and prediction of fatigue strength. Eng Fract Mech 2018;187:165–89. http://dx.doi.org/10.1016/j.engfracmech.2017.11.002.

[3] Masuo H, Tanaka Y, Morokoshi S, Yagura H, Uchida T, Yamamoto Y, Murakami Y. Influence of defects, surface roughness and HIP on the fatigue strength of Ti-6Al-4V manufactured by additive manufacturing. Int J Fatigue 2018;117:163–79. http://dx.doi.org/10.1016/j.ijfatigue.2018.07.020, URL https://linkinghub.elsevier.com/retrieve/pii/S0142112318303050.

[4] Sanaei N, Fatemi A. Defects in additive manufactured metals and their effect on fatigue performance: A state-of-the-art review. Prog Mater Sci 2021;117:100724. http://dx.doi.org/10.1016/J.PMATSCI.2020.100724.

[5] Nezhadfar P, Thompson S, Saharan A, Phan N, Shamsaei N. Structural integrity of additively manufactured aluminum alloys: Effects of build orientation on microstructure, porosity, and fatigue behavior. Addit Manuf 2021;47:102292. http://dx.doi.org/10.1016/j.addma.2021.102292, URL https://linkinghub.elsevier.com/retrieve/pii/S2214860421004528.

[6] Sausto F, Carrion P, Shamsaei N, Beretta S. Fatigue failure mechanisms for AlSi10Mg manufactured by L-PBF under axial and torsional loads: The role of defects and residual stresses. Int J Fatigue 2022;162:106903. http://dx.doi.org/10.1016/j.ijfatigue.2022.106903, URL https://linkinghub.elsevier.com/retrieve/pii/S0142112322001736.

[7] Murakami Y. Metal fatigue: effects of small defects and nonmetallic inclusions. Academic Press; 2019.

[8] Wycisk E, Solbach A, Siddique S, Herzog D, Walther F, Emmelmann C. Effects of defects in laser additive manufactured Ti-6Al-4V on fatigue properties. Phys Procedia 2014;56:371–8. http://dx.doi.org/10.1016/j.phpro.2014.08.120, URL https://linkinghub.elsevier.com/retrieve/pii/S187538921400265X.

[9] Beretta S, Romano S. A comparison of fatigue strength sensitivity to defects for materials manufactured by AM or traditional processes. Int J Fatigue 2017;94:178–91. http://dx.doi.org/10.1016/j.ijfatigue.2016.06.020.

[10] Tridello A, Boursier Niutta C, Rossetto M, Berto F, Paolino D. Statistical estimation of fatigue design curves from datasets involving failures from defects. Int J Fatigue 2023;176:107882. http://dx.doi.org/10.1016/j.ijfatigue.2023.107882, URL https://www.sciencedirect.com/science/article/pii/S0142112323003833.

[11] Qiu C, Panwisawas C, Ward M, Basoalto HC, Brooks JW, Attallah MM. On the role of melt flow into the surface structure and porosity development during selective laser melting. Acta Mater 2015;96:72–9. http://dx.doi.org/10.1016/j.actamat.2015.06.004, URL https://linkinghub.elsevier.com/retrieve/pii/S1359645415003870.

[12] Zhao C, Fezzaa K, Cunningham RW, Wen H, De Carlo F, Chen L, Rollett AD, Sun T. Real-time monitoring of laser powder bed fusion process using high-speed X-ray imaging and diffraction. Sci Rep 2017;7(1):3602. http://dx.doi.org/10.1038/s41598-017-03761-2, URL https://www.nature.com/articles/s41598-017-03761-2.

[13] Leung CLA, Marussi S, Atwood RC, Towrie M, Withers PJ, Lee PD. In situ X-ray imaging of defect and molten pool dynamics in laser additive manufacturing. Nat Commun 2018;9(1):1355. http://dx.doi.org/10.1038/s41467-018-03734-7, URL https://www.nature.com/articles/s41467-018-03734-7.

[14] Zhang J, Song B, Wei Q, Bourell D, Shi Y. A review of selective laser melting of aluminum alloys: Processing, microstructure, property and developing trends. J Mater Sci Technol 2019;35(2):270–84. http://dx.doi.org/10.1016/j.jmst.2018.09.004, URL https://linkinghub.elsevier.com/retrieve/pii/S1005030218301804.

[15] International A. ASTM E3166-20 standard guide for nondestructive examination of metal additively manufactured aerospace parts after build. 2020.

[16] ECSS Secretariat, ESA-ESTEC Requirements & Standards Division. ECSS-Q-ST-70-80C - space product assurance - processing and quality assurance requirements for metallic powder bed fusion technologies for space applications. 2021.

[17] Zhou X, Dai N, Chu M, Wang L, Li D, Zhou L, Cheng X. X-ray CT analysis of the influence of process on defect in Ti-6Al-4V parts produced with selective laser melting technology. Int J Adv Manuf Technol 2020;106(1–2):3–14. http://dx.doi.org/10.1007/s00170-019-04347-0, URL http://link.springer.com/10.1007/s00170-019-04347-0.

[18] du Plessis A, Yadroitsava I, Yadroitsev I. Effects of defects on mechanical properties in metal additive manufacturing: A review focusing on X-ray tomography insights. Mater Des 2020;187:108385. http://dx.doi.org/10.1016/j.matdes.2019.108385, URL https://linkinghub.elsevier.com/retrieve/pii/S0264127519308238.

[19] Romano S, Abel A, Gumpinger J, Brandão AD, Beretta S. Quality control of AlSi10Mg produced by SLM: Metallography versus CT scans for critical defect size assessment. Addit Manuf 2019;28(February):394–405. http://dx.doi.org/10.1016/j.addma.2019.05.017.

[20] Sanaei N, Fatemi A, Phan N. Defect characteristics and analysis of their variability in metal L-PBF additive manufacturing. Mater Des 2019;182:108091. http://dx.doi.org/10.1016/j.matdes.2019.108091.

[21] Wu Z, Wu S, Bao J, Qian W, Karabal S, Sun W, Withers PJ. The effect of defect population on the anisotropic fatigue resistance of AlSi10Mg alloy fabricated by laser powder bed fusion. Int J Fatigue 2021;151:106317. http://dx.doi.org/10.1016/j.ijfatigue.2021.106317.

[22] Shahabi M, Reddy T, Rollett AD, Narra SP. A statistical approach to determine data requirements for part porosity characterization in laser powder bed fusion additive manufacturing. Mater Charact 2022;190:112027. http://dx.doi.org/10.1016/j.matchar.2022.112027.

[23] Kousoulas P, Guo Y. On the probabilistic prediction for extreme geometrical defects induced by laser-based powder bed fusion. CIRP J Manuf Sci Technol 2023;41:124–34. http://dx.doi.org/10.1016/j.cirpj.2022.11.024, URL https://www.sciencedirect.com/science/article/pii/S1755581722002024.

[24] Murakami Y. Inclusion rating by statistics of extreme values and its application to fatigue strength prediction and quality control of materials. J Res Natl Inst Stand Technol 1994;99(4).

[25] Beretta S. More than 25 years of extreme value statistics for defects: Fundamentals, historical developments, recent applications. Int J Fatigue 2021;151:106407. http://dx.doi.org/10.1016/J.IJFATIGUE.2021.106407.

[26] Minerva G, Awd M, Tenkamp J, Walther F, Beretta S. Machine learning-assisted extreme value statistics of anomalies in AlSi10Mg manufactured by L-PBF for robust fatigue strength predictions. Mater Des 2023;235:112392. http://dx.doi.org/10.1016/j.matdes.2023.112392, URL https://www.sciencedirect.com/science/article/pii/S0264127523008079.

[27] Poudel A, Yasin MS, Ye J, Liu J, Vinel A, Shao S, Shamsaei N. Feature-based volumetric defect classification in metal additive manufacturing. Nat Commun 2022;13(1):6369. http://dx.doi.org/10.1038/s41467-022-34122-x, URL https://www.nature.com/articles/s41467-022-34122-x.

[28] Ye J, Poudel A, Liu J, Vinel A, Silva D, Shao S, Shamsaei N. Machine learning augmented X-ray computed tomography features for volumetric defect classification in laser beam powder bed fusion. Int J Adv Manuf Technol 2023;126(7–8):3093–107. http://dx.doi.org/10.1007/s00170-023-11281-9, URL https://link.springer.com/10.1007/s00170-023-11281-9.

[29] Vandecasteele M, Heylen R, Iuso D, Thanki A, Philips W, Witvrouw A, Verhees D, Booth BG. Towards material and process agnostic features for the classification of pore types in metal additive manufacturing. Mater Des 2023;227:111757. http://dx.doi.org/10.1016/j.matdes.2023.111757, URL https://linkinghub.elsevier.com/retrieve/pii/S0264127523001727.

[30] Altmann ML, Benthien T, Ellendt N, Toenjes A. Defect classification for additive manufacturing with machine learning. Materials 2023;16(18). http://dx.doi.org/10.3390/ma16186242, URL https://www.mdpi.com/1996-1944/16/18/6242.

[31] Le V-D, Pessard E, Morel F, Prigent S. Fatigue behaviour of additively manufactured Ti-6Al-4V alloy: The role of defects on scatter and statistical size effect. Int J Fatigue 2020;140:105811.

[32] Miner JP, Ngo A, Gobert C, Reddy T, Lewandowski JJ, Rollett AD, Beuth J, Narra SP. Impact of melt pool geometry variability on lack-of-fusion porosity and fatigue life in powder bed fusion-laser beam Ti–6Al–4V. Addit Manuf 2024;95:104506.

[33] Snow Z, Scime L, Ziabari A, Fisher B, Paquit V. Observation of spatter-induced stochastic lack-of-fusion in laser powder bed fusion using in situ process monitoring. Addit Manuf 2023;61:103298.

[34] Kim T, Kim M-K, Fang Y, Suhr J. Moisture effects on qualities and properties of laser powder bed fusion (LPBF) additive manufacturing of as-built 17-4PH stainless steel parts. Metals 2023;13(9):1550.

[35] ASTM E466-21 standard practice for conducting force controlled constant amplitude axial fatigue tests of metallic materials. 2021.

[36] Beretta S, Patriarca L, Gargourimotlagh M, Hardaker A, Brackett D, Salimian M, Gumpinger J, Ghidini T. A benchmark activity on the fatigue life assessment of AlSi10Mg components manufactured by L-PBF. Mater Des 2022;218:110713. http://dx.doi.org/10.1016/j.matdes.2022.110713, URL https://linkinghub.elsevier.com/retrieve/pii/S0264127522003355.

[37] Beretta S, Anderson C, Murakami Y. Extreme value models for the assessment of steels containing multiple types of inclusion. Acta Mater 2006;54(8):2277–89. http://dx.doi.org/10.1016/j.actamat.2006.01.016, URL https://linkinghub.elsevier.com/retrieve/pii/S1359645406000814.

[38] Reiss R-D, Thomas M, Reiss R. Statistical analysis of extreme values. Vol. 2, Springer; 1997.

[39] Beretta S. Affidabilità delle costruzioni meccaniche: Strumenti e metodi per l'affidabilità di un progetto. Springer Science & Business Media; 2010.

[40] Coles S. An introduction to statistical modeling of extreme values. Springer series in statistics, London: Springer London; 2001, http://dx.doi.org/10.1007/978-1-4471-3675-0.

[41] Romano S, Brandão A, Gumpinger J, Gschweitl M, Beretta S. Qualification of AM parts: Extreme value statistics applied to tomographic measurements. Mater Des 2017;131:32–48. http://dx.doi.org/10.1016/j.matdes.2017.05.091.

[42] Murakami Y. Material defects as the basis of fatigue design. Int J Fatigue 2012;41:2–10. http://dx.doi.org/10.1016/j.ijfatigue.2011.12.001, URL https://linkinghub.elsevier.com/retrieve/pii/S0142112311003161.

[43] Yadollahi A, Mahtabi MJ, Khalili A, Doude HR, Newman JC. Fatigue life prediction of additively manufactured material: Effects of surface roughness, defect size, and shape. Fatigue Fract Eng Mater Struct 2018. http://dx.doi.org/10.1111/ffe.12799.

[44] Shiozawa K, Lu L. Effect of non-metallic inclusion size and residual stresses on gigacycle fatigue properties in high strength steel. Adv Mater Res 2008;44–46:33–42. http://dx.doi.org/10.4028/www.scientific.net/AMR.44-46.33, URL https://www.scientific.net/AMR.44-46.33.

[45] Tenkamp J, Stern F, Walther F. Uniform fatigue damage tolerance assessment for additively manufactured and cast Al-Si alloys: An elastic-plastic fracture mechanical approach. Addit Manuf Lett 2022;3:100054. http://dx.doi.org/10.1016/j.addlet.2022.100054, URL https://linkinghub.elsevier.com/retrieve/pii/S2772369022000287.

[46] Tenkamp J, Stammkötter S, Walther F. Qualification of uniform fatigue damage tolerance law for additively manufactured and cast Al-Si alloys. Procedia Struct Integr 2022;42:328–35. http://dx.doi.org/10.1016/j.prostr.2022.12.040, URL https://linkinghub.elsevier.com/retrieve/pii/S2452321622005972.

[47] Sausto F, Tezzele C, Beretta S. Analysis of fatigue strength of L-PBF AlSi10Mg with different surface post-processes: Effect of residual stresses. Metals 2022;12(6):898. http://dx.doi.org/10.3390/met12060898, URL https://www.mdpi.com/2075-4701/12/6/898.

[48] Zio E. Monte Carlo simulation: The method. Springer; 2013.